ARL-TR-9290 ● SEP 2021

Rapid and Low-Cost Synthesis of Porous Silicon Powder from Mg_2Si for Energetic Applications

by Nathan A Banek, Dustin T Abele, Katherine M Price, Philip M Guerieri, Wayne A Churaman, and Michael J Wagner

ARL-TR-9290 ● SEP 2021

Rapid and Low-Cost Synthesis of Porous Silicon Powder from Mg_2Si for Energetic Applications

Nathan A Banek, Philip M Guerieri, and Wayne A Churaman
Sensors and Electron Devices Directorate, DEVCOM Army Research Laboratory

Katherine M Price
Fibertek

Dustin T Abele and Michael J Wagner
The George Washington University

REPORT DOCUMENTATION PAGE	*Form Approved* *OMB No. 0704-0188*

1. REPORT DATE *(DD-MM-YYYY)*	**2. REPORT TYPE**	**3. DATES COVERED (From - To)**
September 2021	Technical Report	August 2020–August 2021

4. TITLE AND SUBTITLE

Rapid and Low-Cost Synthesis of Porous Silicon Powder from Mg_2Si for Energetic Applications

5a. CONTRACT NUMBER

5b. GRANT NUMBER

5c. PROGRAM ELEMENT NUMBER

6. AUTHOR(S)

Nathan A Banek, Dustin T Abele, Katherine M Price, Philip M Guerieri, Wayne A Churaman, and Michael J Wagner

5d. PROJECT NUMBER

5e. TASK NUMBER

5f. WORK UNIT NUMBER

7. PERFORMING ORGANIZATION NAME(S) AND ADDRESS(ES)

DEVCOM Army Research Laboratory
ATTN: FCDD-RLS-EM
Adelphi, MD 20783-1138

8. PERFORMING ORGANIZATION REPORT NUMBER

ARL-TR-9290

9. SPONSORING/MONITORING AGENCY NAME(S) AND ADDRESS(ES)

10. SPONSOR/MONITOR'S ACRONYM(S)

11. SPONSOR/MONITOR'S REPORT NUMBER(S)

12. DISTRIBUTION/AVAILABILITY STATEMENT

Approved for public release: distribution unlimited.

13. SUPPLEMENTARY NOTES

ORCID IDs: Nathan Banek, 0000-0001-7652-5530; Dustin Abele, 0000-0003-4888-0556; Katherine Price, 0000-0001-6120-0020; Philip Guerieri, 0000-0001-6145-993X; Wayne Churaman, 0000-0002-5070-1695; Michael Wagner 0000-0001-9559-7804

14. ABSTRACT

Porous silicon (Si) powder filled with sodium perchlorate oxidizer is a promising energetic material for advanced propellant and explosive formulations. Currently, porous Si powder is derived from p-type Si wafers etched in 3:1 concentrated hydrofluoric acid:ethanol solution followed by a liftoff procedure. This process is fundamentally expensive due to the cost of p-type Si wafers. An alternative method to generate porous Si powder from Mg_2Si with similar properties to anodically etched porous Si is presented. Flame-speed measurements were performed and calculated to be comparable to anodically etched Si up to 977 m/s. Without the use of hydrofluoric acid or p-type wafers, this is a safer and cost-efficient way to produce porous Si for energetic applications.

15. SUBJECT TERMS

silicon, Si, porous silicon, energetic materials, magnesium silicide, h-terminated silicon

16. SECURITY CLASSIFICATION OF:			**17. LIMITATION OF ABSTRACT**	**18. NUMBER OF PAGES**	**19a. NAME OF RESPONSIBLE PERSON**
a. REPORT	**b. ABSTRACT**	**c. THIS PAGE**			Nathan A Banek
Unclassified	Unclassified	Unclassified	UU	24	**19b. TELEPHONE NUMBER (Include area code)** (301) 304-0952

Standard Form 298 (Rev. 8/98)
Prescribed by ANSI Std. Z39.18

Contents

List of Figures

1. Introduction

Porous silicon (pSi) research is receiving much interest for its potential use in a variety of applications including sensors, imaging, biological drug delivery, anti-reflective coatings, lithium-ion battery anodes, and energetic materials.[1–6] A variety of methods have been demonstrated to prepare pSi with different porosities including stain etching, vapor etching, metal-assisted etching, salt templating, and magnesiothermic reduction.[7] However, few methods produce microporous pSi with pore sizes near or less than 2 nm (as defined by The International Union of Pure and Applied Chemistry). This "nanoporous" form of Si inherently has high specific surface area (>600 m^2/g) and high porosity (>50%), making it a desirable material for energetic, catalysis, hydrogen (H) storage, sensors, and drug-delivery applications.

The most commonly used method to prepare nanoporous pSi is by anodic or galvanic etching of p-type Si wafers in hydrofluoric acid (HF)-containing electrolyte.[8] When Si is immersed in an HF solution, the surface is left terminated with H bonds. A large specific surface area of pSi produced by these etching methods directly correlates to a large Si-H_x to Si ratio. Such termination is advantageous for subsequent hydrosilylation functionalization for drug-delivery applications[9] or use as-is in energetic applications, as it has been determined the H termination is crucial to reacting with strong oxidizers.[10] When impregnated with sodium perchlorate ($NaClO_4$), flame speeds up to 3000 m/s have been reported upon ignition for on-chip devices due to the high porosity and small average pore size of pSi.[11] Using p-type Si wafers to produce pSi by anodic-etching favors specific applications such as on-chip energetics. With the relatively high flame speed of pSi compared with other energetic materials, a powder form could find expanded use when added to traditional propellants to increase energy density. A liftoff procedure is performed to isolate pSi flakes from the wafer to produce pSi powder when ground and agitated by ultrasonication.[12] However, production from costly p-type Si wafers limits applications to small scales (e.g., igniters, where production is considered cost-effective).

A scaled-up manufacturing method for pSi microparticles with ample specific surface area can significantly open potential applications to larger propellant and explosive formulations. Therefore, developing a new method to produce pSi is of interest where cost and scalability is especially important. The use of p-type Si is fundamentally expensive due to wafer processing and by the loss of Si from top-down etching to generate pores. Bottom-up production Si from low-cost precursors is a more scalable and affordable method. Si-containing Zintl phases are one such material that has been shown to produce Si nanomaterials.[13] However, there are no reports of Si produced from Zintl phases with comparable surface area and porosity to anodic-etched Si; neither do they have the required H-terminated surface. Previously, it was demonstrated that magnesium silicide (Mg_2Si) is reactive with aluminum (Al) halides at temperatures as low as 125 °C when Mg_2Si was reacted with aluminum bromide ($AlBr_3$) in toluene.[14] The reaction was time-consuming, requiring 24 h of reacting and produced crystalline Si nanoparticles in high yield around 50 nm with no noticeable porosity. In attempt to lower the production cost of Si, a solvent-free method will be demonstrated at 125 ℃ exploiting the eutectic of 0.6 $AlCl_3$ and 0.4 NaCl at 111 ℃.[15] The pSi exhibited a high specific surface area of 768 ± 9 m^2/g with 2- to 7-nm pore size and evidence of hydrogen termination without the use of HF. After the pores were filled with $NaClO_4$ oxidizer, the particles were ignited when heated by nichrome (NiCr) wire with measured flames speeds up to 977 m/s, comparable to particles produced from Si wafers by anodic etching (981 m/s).

2. Experimental

2.1 Porous Si Synthesis

2.1.1 Porous Si from Mg_2Si

To remove minor crystalline Si impurities, the Mg_2Si starting material was reacted with Mg metal prior to its use as a reagent. In an argon (Ar) atmosphere drybox (<1 ppm H_2O and O_2 content), 1.8 g Mg_2Si (99.99%, Alfa Aesar) were mixed with 200 mg Mg powder (99.8%, Alfa Aesar) in a 15-mL stainless steel capsule with a 1-cm stainless steel ball at 30 Hz for 10 min with a Fritsch Pulverisette 10 minimill to generate a fine powder. The powder was placed into a carbon boat (5 mL) and inserted into a quartz tube that was further sealed with an O-ring and borosilicate caps held by steel clamps. The contents were left under Ar gas and the pressure of the dry box (slightly greater than 1 atm) and heated in a horizontal tube furnace from room temperature at 20 ºC/min, then held at 675 °C for 2 h. After cooling naturally, the tube was brought back into the Ar drybox and stored until further use.

Powders of 0.367 g (4.79 mmol) Mg_2Si (99.9%, Alfa Aesar), 10.85 g (81.4 mmol) $AlCl_3$ (Alfa Aesar, 99.985%), and 2.38 g (40.7 mmol) NaCl (99.9% previously dried at 300 ℃, Fisher Scientific) were combined into a 80-mL hardened steel ball mill cup with ten 1-cm hardened steel balls for a ball to powder ratio of 10:1. The cup was sealed with a Viton O-ring and lid, then sealed additionally with electrical tape to help prevent air and moisture from contaminating the contents. The materials were lightly milled for 30 min at 200 rpm, after which the cup was brought back into the dry box and the contents were removed. Then 13 g of the powder were transferred into a round bottom flask and sealed with a rubber septum. The contents were placed under a flowing Ar stream through the flask septum with a needle to ensure any generated pressure would not dislodge the septum from the flask and expose the contents to air atmosphere. The flask was then submerged in an oil bath, preheated to 125 °C, to allow the $AlCl_3$ and NaCl contents to become molten. After the contents were liquid, the stir plate was turned on to mix the reactants for 5 min. Then the flask was removed from the oil bath and let cool naturally. The flask was then placed into an ice bath and 200 mL degassed methanol (99.8%, Fisher Scientific) was added to the flask and stirred until gas ceased to evolve. Ten milliliters of concentrated HCl (VWR Life Science) were added and let stir for an additional 10 min. The sample was recovered by vacuum filtration and then placed into 150 mL of degassed H_2O and agitated by sonication for 30 s to dissolve remaining salts, then recovered immediately by vacuum filtration and further washed with methanol. The product was dried under dynamic vacuum and stored in a N_2-filled drybox until further use.

2.1.2 Porous Si by Anodic Etching

Anodically etched pSi (AE-pSi) was used for comparison. It was produced from a platinum-backed p-type Si wafer (6–9 ohm-cm) etched in a 3:1 concentrated HF: ethanol (200 proof) solution at 18 mA/cm^2 current density for 3 h. After that, a liftoff procedure was performed at a current of 90 mA/cm^2, which dissolved the interface between the AE-pSi and the unetched wafer to generate free-standing AE-pSi flakes. The flakes were collected, rinsed thoroughly with methanol, and let dry under N_2 gas for 24 h. The flakes were lightly ground in a mortar and pestle until a powder was obtained and transferred to a 200-mL beaker containing 150 mL of absolute ethanol. A sonication horn was submerged in the solution and set to 100% duty cycle at 75% output for 2 h. The AE-pSi particles were collected by centrifugation and let dry under N_2 for 24 h.

2.2 Energetic Testing

Flame-speed measurements were performed by placing a small quantity (<10 mg) of pSi powder into a 3D-printed trench with a cavity measuring 20 × 1.5 × 1 mm. The pSi was wet with methanol to allow the sample to pack naturally. After the pSi dried, the combined weight was recorded to obtain the pSi weight. The trench was then placed into an N_2-containing chamber with a NiCr wire embedded in the pSi powder at one end of the trench. Oxidizer (3.2 M $NaClO_4$ in methanol) was added to the trench sufficient to saturate the pSi powder and let dry for 15 min under N_2 flowing through the chamber. Ignition was triggered by a 4 A square-wave current pulse (0.1 s) delivered from a Quantum Composers 9730 series pulse generator with the trigger signal split to a Photon FASTCAM SA5 to record the ignition. Flame-speed measurements were performed using ImageJ (www.imagej.net) by measuring the flame propagating along the trench gap opening with respect to the time evolved per ensuing frame recorded. Camera data were recorded at 192 × 32 pixels at a frame rate of 500,000 s^{-1}.

2.3 Surface Area and Porosity

Surface area was determined from N_2 adsorption isotherms obtained with a Tri-Star 3000 (Micrometrics). One of the three sample measurement ports of the Tri-Star was equipped with an empty sample tube with which the saturation vapor pressure (P0) of N_2 was measured concurrently with each measurement of the equilibrium vapor pressure over the sample. Surface area calculations were performed with the Brunauer–Emmett–Teller equation, and porosity measurements were calculated using N_2 desorption data.

2.4 Fourier-Transform Infrared Spectroscopy (FTIR)

Infrared spectra were collected by a PerkinElmer Spectrum One using a liquid-N_2-cooled MCT (mercury–cadmium–telluride) detector in attenuated total reflection (ATR) mode with a diamond reflection crystal.

2.5 Powder X-Ray Diffraction (XRD)

XRD patterns were obtained with a Bruker D2 Phaser diffractometer using copper Kα radiation. A zero-background quartz sample plate was used for spectra collection.

2.6 Scanning Electron Microscopy (SEM)

SEM micrographs were obtained using an FEI Teneo LV with its in-lens secondary electron detector using 2-kV accelerating voltage.

3. Results and Discussion

3.1 Crystalline Phase and Crystallite Size

The preparation of the two pSi powders differed greatly, and the pore formation mechanism was entirely different, thus the properties related to favorable energetic applications may be observable through material analysis. AE-pSi was observed as crystalline by XRD with two crystallite sizes. Sharp peaks appeared at 28.44°, 47.3°, 56.12°, and 69.13° that match the Si reference pattern for 111, 220, 311, and 400 reflections, respectively. Additionally peaks appearing at 26° and 43° were unidentifiable impurities. Broader peaks appeared below the sharp peaks indicative of nanocrystals within the sample (Fig. 1). The nanocrystallite size was estimated at 4 nm using Sherrer's equation.[16] The larger crystals are likely the byproduct of using a crystalline wafer where large crystal impurities may have broken off near the edge of the pSi/Si interface while performing the liftoff procedure. The porous Si produced from Mg_2Si appeared as amorphous, most likely the result of the low temperature and short reaction time to produce elemental Si from Mg_2Si oxidation. The peak at 28° is asymmetric with fronting at lower angles indicative of some surface oxide.

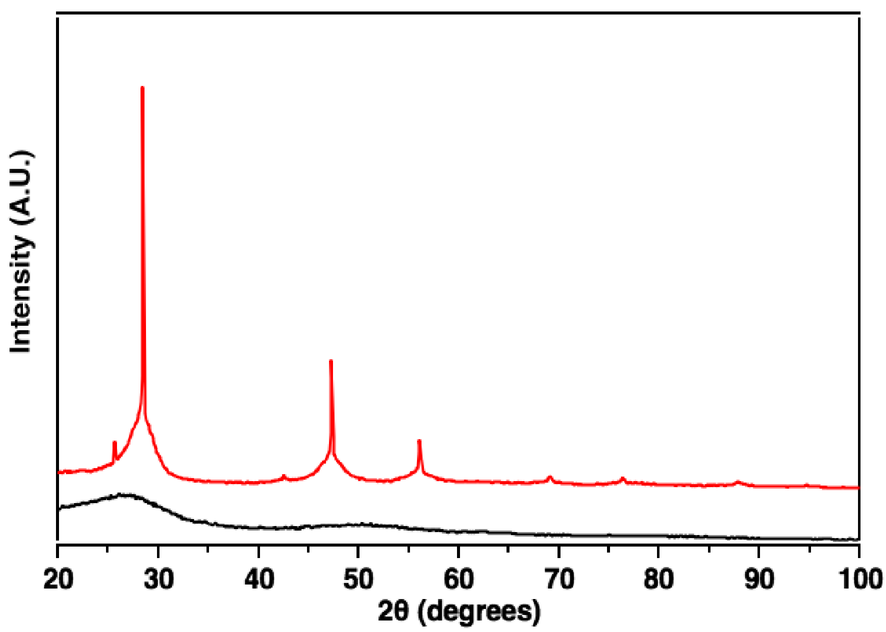

Fig. 1 Powder XRD patterns of pSi produced (black/bottom) from Mg_2Si and (red/top) by anodic etching of p-type Si wafer

3.2 Particle Size and Morphology

The purified pSi product from Mg_2Si consists of particles ranging from a few hundred nanometers to 5 µm in size, with most particles between 1 and 2 µm (Fig. 2). The size of the pSi produced from Mg_2Si is a direct result of the Mg_2Si particle size. No attempt to control the particle size or size exclusion methods was performed. Particle morphology was irregular with sharp edges and flat surfaces. In contrast to the particle formation from Mg_2Si, AE-pSi particles are formed after the liftoff procedure, ground, and subsequently sonicated in ethanol. Their size is notably larger with a broader distribution. Most particles appeared between 10 to 15 µm in size with some larger particles 20 to 30 µm (Fig. 3).

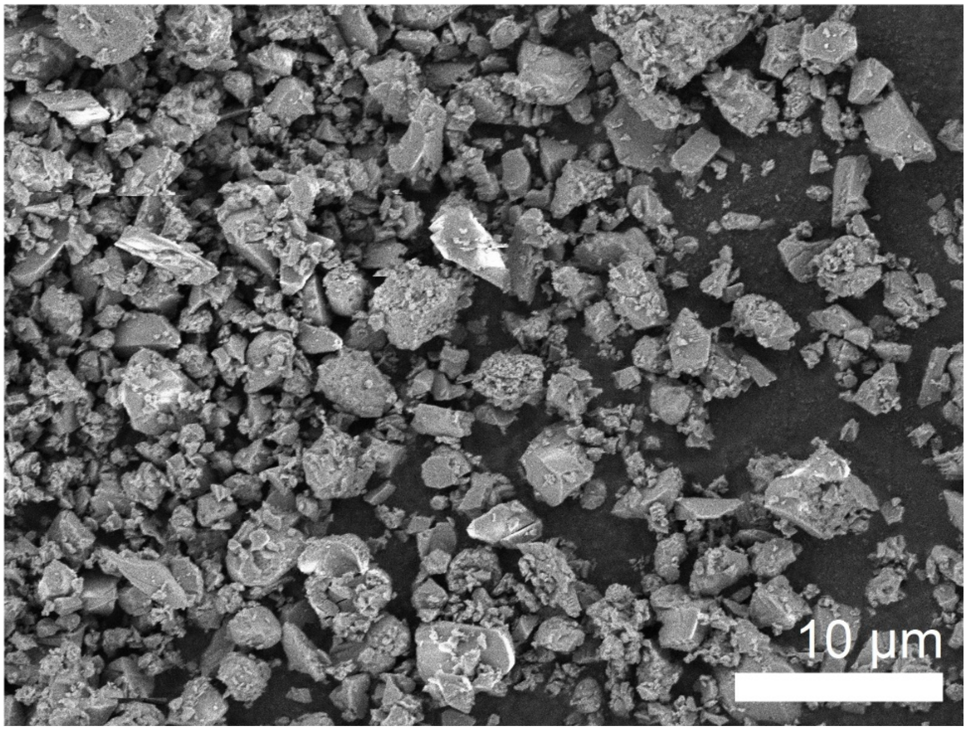

Fig. 2 SEM image of pSi particles produced from Mg_2Si

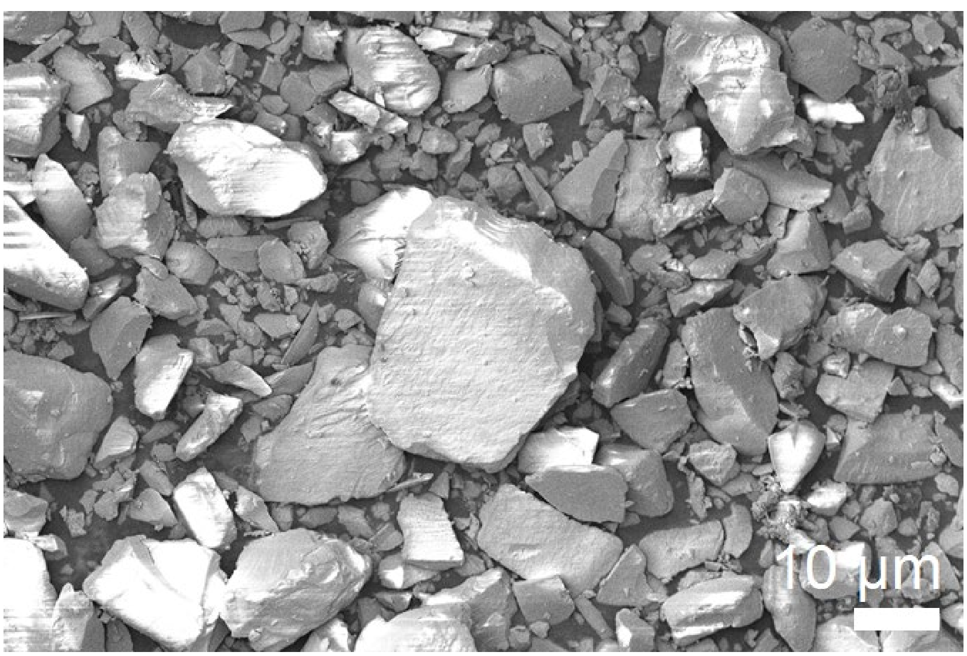

Fig. 3 SEM image of pSi particles produced by anodic etching of p-type Si wafer

3.3 Surface Area and Porosity

The pSi from Mg_2Si had a surface area measured at 768 ± 4 m^2/g, greater than AE-pSi at 677 ± 7 m^2/g (the N_2 isotherms appear in Fig. 4). However, pSi from Mg_2Si had a lower pore volume of 0.665 cm^2/g (0.943 cm^2/g for AE-pSi) and larger average pore size of 4.3 nm (3.4 nm for AE-pSi) (Fig. 5). The larger surface area with respect to porosity could be attributed to the smaller particle size of the pSi from Mg_2Si. Their pore size distributions were notably different as well. AE-pSi was produced with a near homogenous network of pores generated by the electrochemical etching procedure at uniformly low current density. The pore size and morphology are not fixed with the electrometrical etching process; however, it becomes relatively specific under these conditions to produce pSi with high surface area. The pore formation for our pSi is a completely different mechanism where the pores are generated from precipitation of Si, Al, and $MgCl_2$ products in a presumably homogenous manner dependent on reactant diffusion.

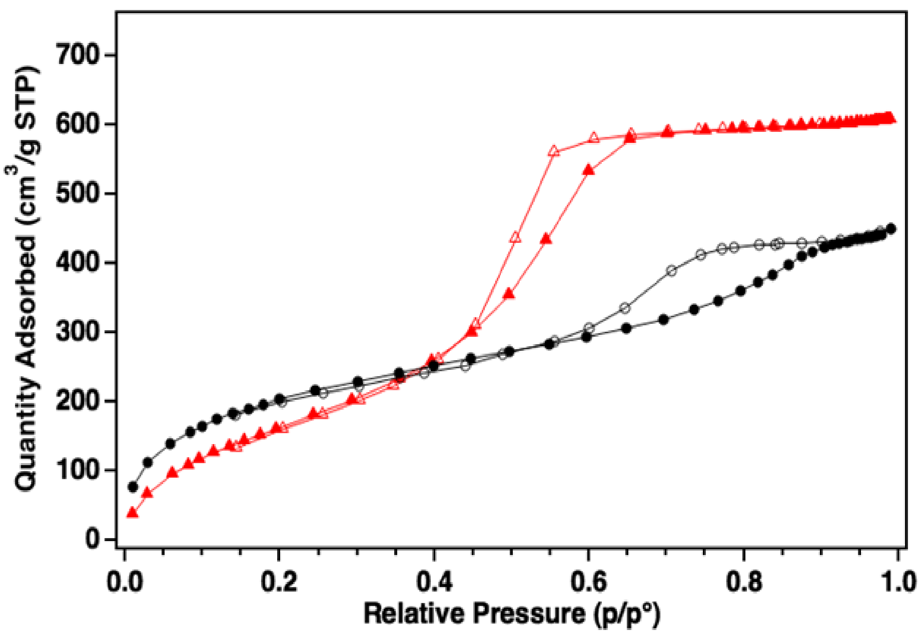

Fig. 4 **N_2 isotherm absorption/desorption data of pSi produced (black circles) from Mg_2Si and (red triangles) by anodic etching of p-type Si wafer. The line connectivity is purely for visual aid.**

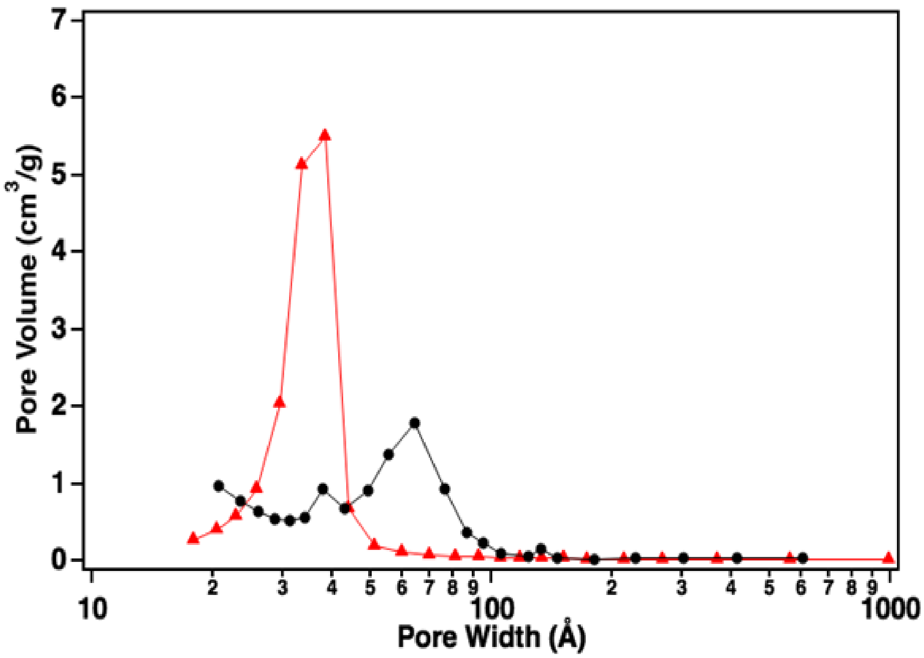

Fig. 5 **N_2 desorption porosity data of pSi produced (black circles) from Mg_2Si and (red triangles) by anodic etching of p-type Si wafer. The line connectivity is purely for visual aid.**

3.4 Hydrogen Surface Termination

Both samples showed evidence of H termination shown by a broad peak at 2100 cm^{-1} in the ATR-FTIR spectrum (Fig. 6). Without exposure to HF, an Si–H bond formation for the pSi from Mg_2Si by the same pathway as AE-pSi is not possible. The only source for H-bonding is H_2 gas evolved during the purification step when the alcohol in presence of $AlCl_3$ reacted with Al.[17] Not all surface bonding is with H; an Si–O–Si stretch is evident at 1100 cm^{-1}. Both samples were exposed to moist air so some hydrolysis will occur, and minor absorbance was measured around 2200 cm^{-1}, indicative of back-bond oxidation.

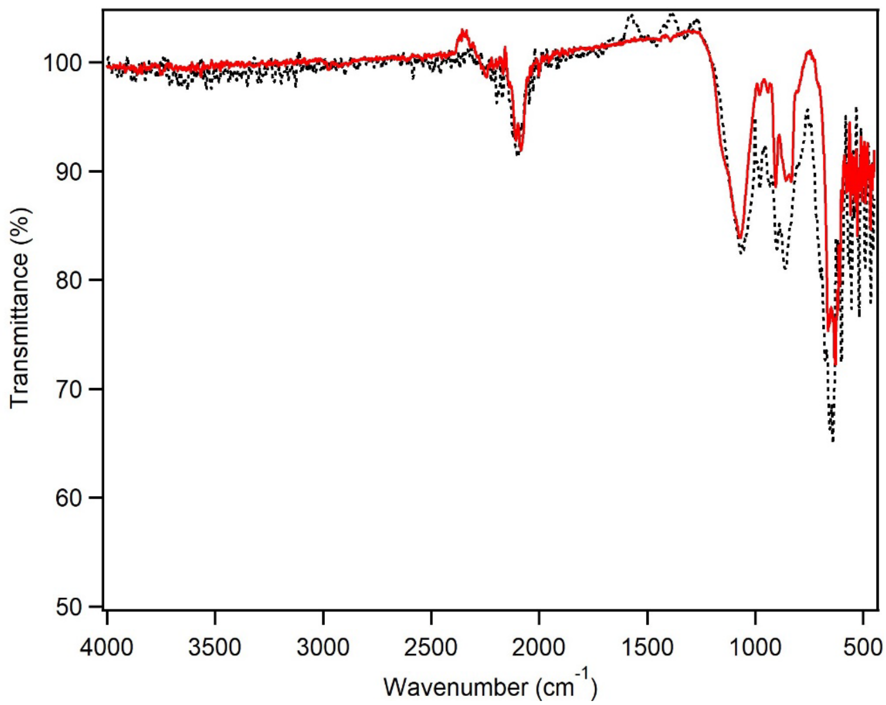

Fig. 6 FTIR of pSi produced (black dashes) from Mg_2Si and (solid red line) by anodic etching of p-type Si wafer

3.5 Oxide Content Determination

A higher surface area should result in a larger oxide content. Thermogravimetric analysis was performed to determine the oxygen mass gain to back-calculate the original stoichiometry. The samples were heated from 30 to 1000 °C at 20 °C/min and were stable in air up to 180 °C when weight gain started to occur (Fig. 7). Both samples oxidized at a similar rate up to 120% of their original mass, which is indicative of their similar surface areas. The AE-pSi oxidation rate slowed, which may be related to its average particle size; larger particles will have longer diffusion distances to their core and may limit the transfer of O from surface to core as SiO_2 builds up on the outside. The pSi from Mg_2Si reached full oxidation around 700 °C while the AE-pSi became fully oxidized closer to 800 °C. The weight gains for pSi from Mg_2Si and AE-pSi were 65% and 72%, which corresponds to an original composition of $SiO_{0.86}$ and $SiO_{0.74}$, respectively.

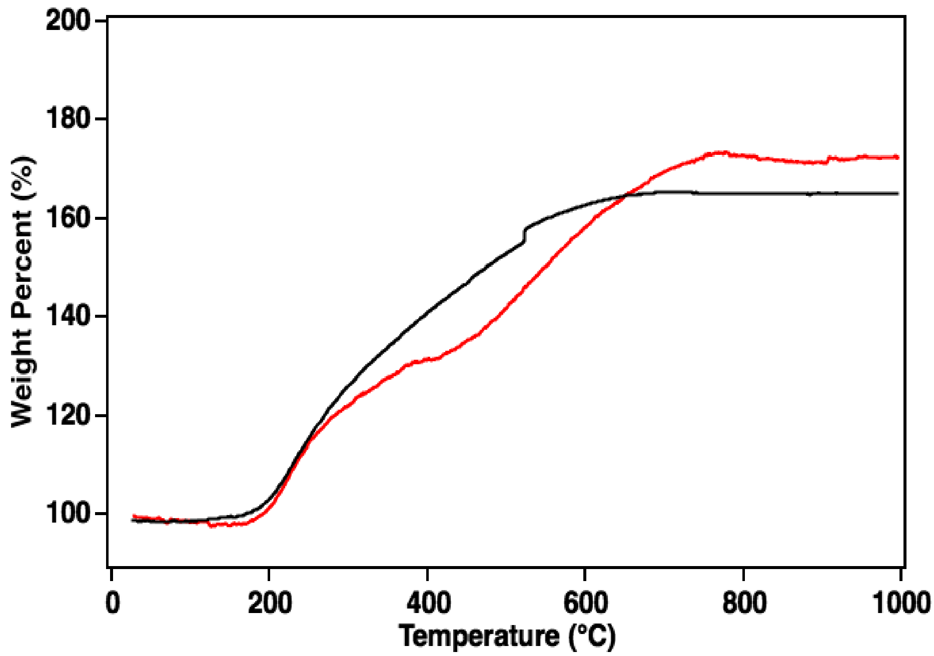

Fig. 7 Thermal gravimetric analysis plot of pSi (black) from Mg_2Si and (red) by anodic etching of p-type Si wafer. The heating rate was 20 °C/min in air.

3.6 Flame-Speed Measurements

The flame-speed testing setup appears in Fig. 8. A NiCr wire is attached to terminals and embedded into the pSi powder prior to adding the oxidizer. A stock reference photo was taken for each test to determine the distance to pixel ratio (example photo in Fig. 8). The flame propagation for pSi from Mg_2Si and AE-pSi was recorded at 1.904 µs intervals with first light set as 0 µs (Figs. 9 and 10, respectively). Velocity measurements were calculated using the slope of the propagation curve, with the first light flame front normalized to 0 mm (Figs. 9 and 10).

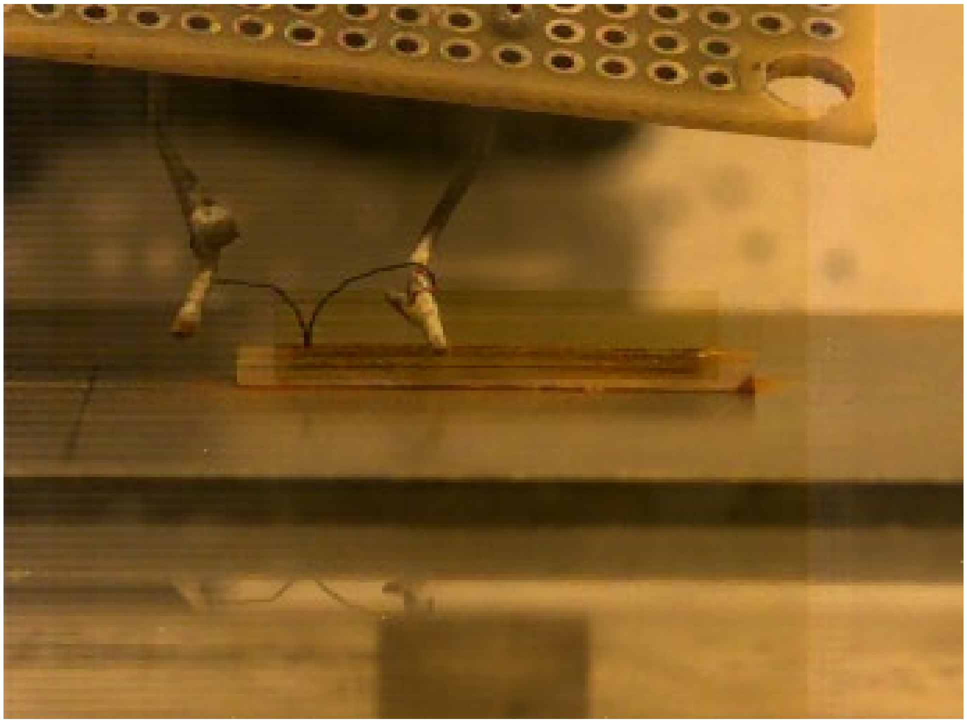

Fig. 8 Representative reference photo of a pSi/$NaClO_4$ sample prior to ignition

Three tests were performed (Figs. 9 and 10) for both pSi and AE-pSi with measured average velocities of 977, 887, and 855 m/s and 981, 974, and 954 m/s, respectively (Figs. 11 and 12). On average, the pSi from Mg_2Si velocity was 7% slower than AE-pSi. We observed inconsistencies in flame-speed linearity for some tests for the pSi from Mg_2Si which we believe is due to the poor packing efficiency when placed into the trench with methanol due to the small particle size, as the particles tend to agglomerate, leaving voids and cracks in the packed particles (Fig. 13). We anticipate that pSi particles from Mg_2Si would pack better and perform more consistently if synthesized as larger particles by using a less intense mixing method for the starting reagents.

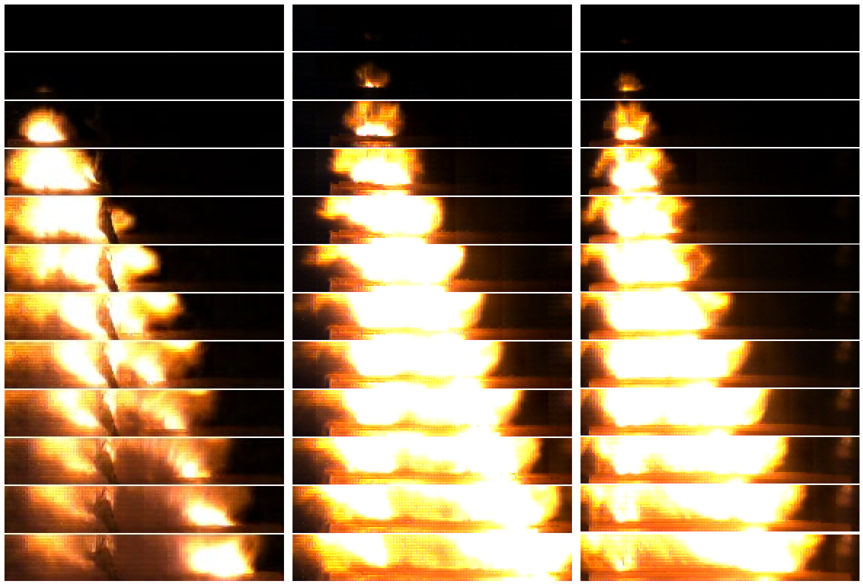

(a) (b) (c)

Fig. 9 Flame propagation frame captures for pSi from Mg_2Si

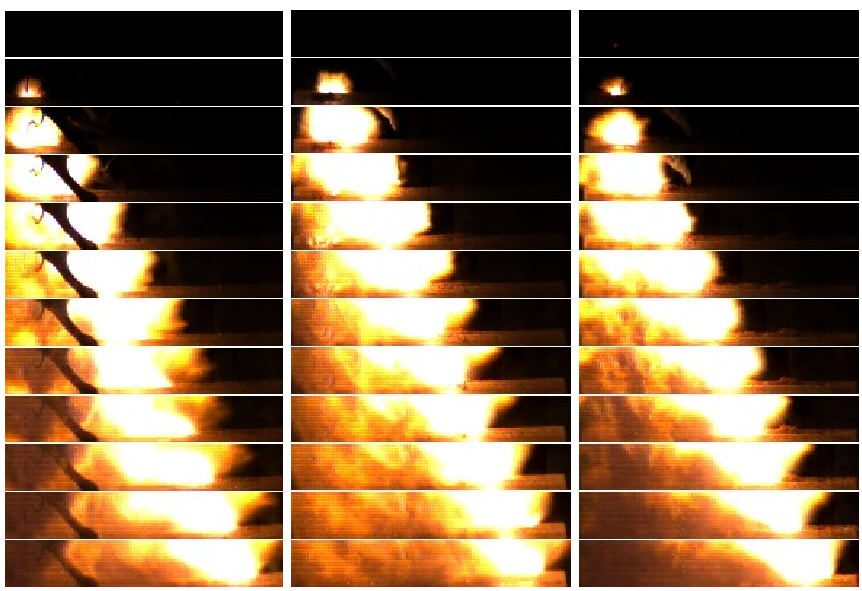

(a) (b) (c)

Fig. 10 Flame propagation frame captures for pSi produced by anodic etching of p-type Si wafer

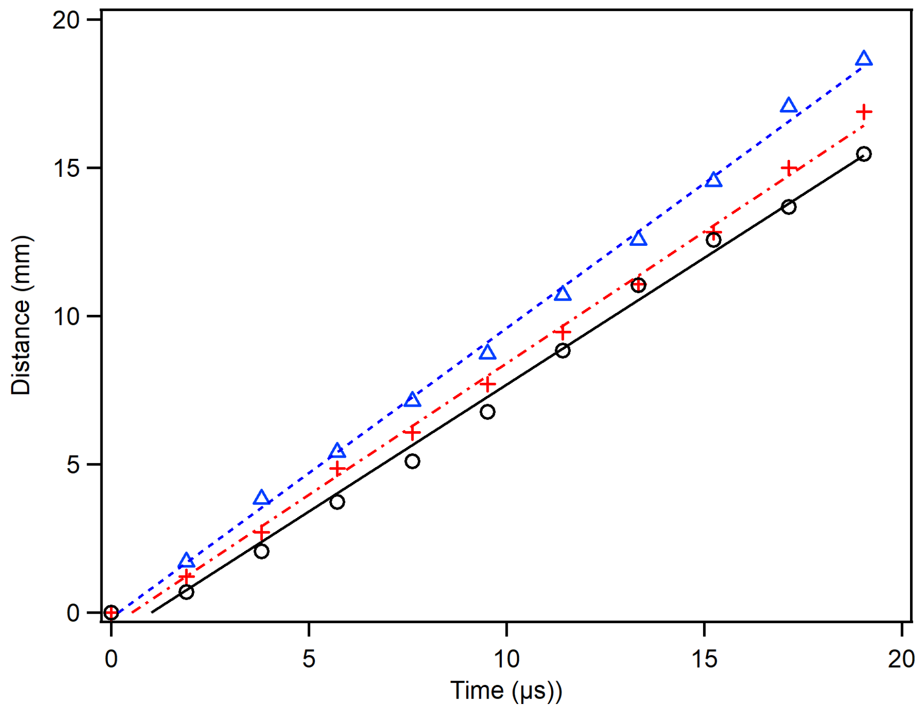

Fig. 11 **Flame-speed average velocity calculations for pSi from Mg_2Si from image in Fig. 9a), blue triangles), 9b) red crosses, and 9c) black circles; linear fits are shown**

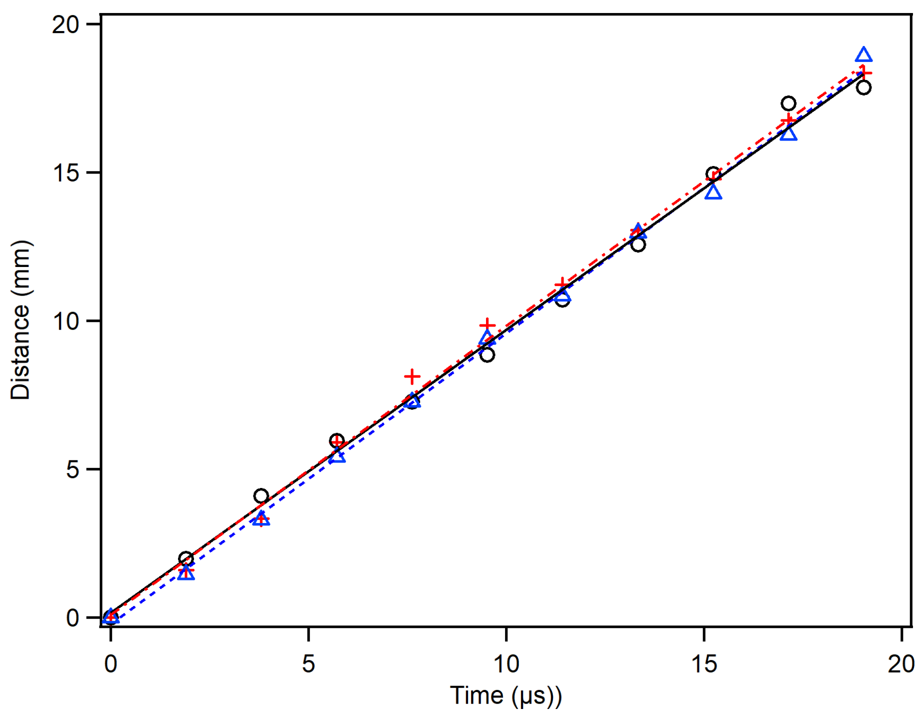

Fig. 12 **Flame-speed average velocity calculations for pSi produced by anodic etching of p-type Si wafer from image in Fig. 10a) blue triangles, 10b) red crosses, 10c) black circles; linear fits are shown**

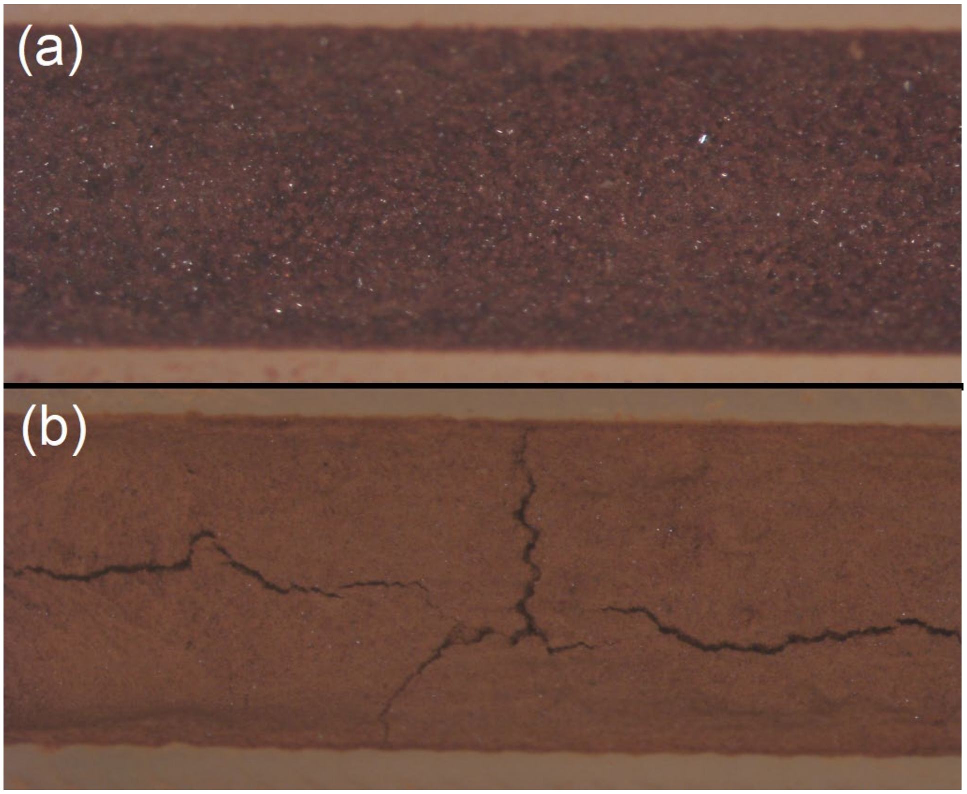

Fig. 13 Microscope image of packing behavior of pSi produced (a) by anodic etching of p-type Si wafer and (b) from Mg_2Si

4. Conclusion

Porous Si particles were fabricated from the reaction between Mg_2Si and $AlCl_3$ in an NaCl/$AlCl_3$ molten salt medium. The particles, despite no exposure to HF, had similar H surface termination to particles produces from the anodic-etching process in 3:1 HF: ethanol. The particles produced from Mg_2Si had a slightly higher surface area but lower pore volume (768 ± 4 vs. 677 ± 7 m^2/g and 0.665 vs. 0.943 cm^3/g, respectively). A peak flame speed of 977 m/s was measured, comparable to anodically etched Si at 981 m/s. The difference in crystallinity and total pore volume did not play a noticeable role in the performance difference, where high surface area and H surface termination is likely to be the most important properties. The average flame speed was measured at 7% lower than anodic-etched Si particles over three comparable flame-speed measurements and may have resulted from some inconsistency in particle packing within the 3D-printed trench. Given the cost effectiveness of this new pSi production method, combined with the lack of HF usage, it is a promising alternative for large-scale production of pSi powders to be used in energetic formulation additives.

5. References

1. Harraz FA. Porous silicon chemical sensors and biosensors: a review. Sensors and Actuators B: Chemical. 2014;202:897–912.

2. Arshavsky-Graham S, Massad-Ivanir N, Segal E, Weiss S. Porous silicon-based photonic biosensors: current status and emerging applications. Analytical Chemistry. 2019;91(1):441–467.

3. Li W, Liu Z, Fontana F, Ding Y, Liu D, Hirvonen JT, Santos HA. Tailoring porous silicon for biomedical applications: from drug delivery to cancer immunotherapy. Advanced Materials. 2018;30:1703740.

4. Wang J, Kumeria T, Teresa Bezem M, Wang J, Sailor MJ. Self-reporting photoluminescent porous silicon microparticles for drug delivery. ACS Applied Materials & Interfaces. 2018;10(4):3200–3209.

5. Dai F, Yi R, Yang H, Zhao Y, Luo L, Gordin ML, Sohn H, Chen S, Wang C, Zhang S, Wang D. Minimized volume expansion in hierarchical porous silicon upon lithiation. ACS Applied Materials & Interfaces. 2019;11(14):13257–13263.

6. Plessis, M. Properties of porous silicon nano-explosive devices. Sensors and Actuators A: Physical. 2007;135(2):666–674.

7. Canham L. Properties of porous silicon. INSPEC, The Institution of Electrical Engineers; 1997.

8. Turner D. J. Electropolishing silicon in hydrofluoric acid solutions. Journal of Electrochemical Society. 1958;5:402.

9. Anglin EJ, Cheng L, Freeman WR, Sailor MJ. Porous silicon in drug delivery devices and materials. Advanced Drug Delivery Reviews. 2008;60(11):1266–1277.

10. Churaman W, Currano L, Singh AK, Rai US, Dubey M, Amirtharaj P, Ray PC. Understanding the high energetic behavior of nano-energetic porous silicon. Chemical Physics Letters. 2008:464(4-6):198–201.

11. Becker CR, Apperson S, Morris CJ, Gangopadhyay S, Currano LJ, Churaman WA, Stoldt CR. Galvanic porous silicon composites for high-velocity nanoenergetics. Nano Letters. 2011;11(2):803–807.

12. Behran J, Tsybeskov L, Fauchet PM. Preparation and characterization of ultrathin porous silicon films. Applied Physical Letters. 1995;66(13):27.

13. Yang CS, Bley RA, Kauzlarich SM, Lee HWH, Delgado GR. Synthesis of alkyl-terminated silicon nanoclusters by a solution route. Journal of the American Chemical Society. 1999;121(22):5191–5195.

14. Banek NA, Hays KA, Wagner MJ. High capacity silicon/multiwall graphene nanoshell Li-ion battery anodes from a low-temperature, high-yield and scalable green synthesis. Journal of Electrochemical Society. 2017;164:A1569.

15. Banek NA, Wagner MJ. The George Washington University, assignee. Low temperature, high yield synthesis of nanomaterials and composites from zintl phases. United State patent application US 2020/0014024 A1. 2020 Jan 9.

16. Scherrer P. Göttinger Nachrichten. Math Phys. 1918;2:98–100.

17. Seri O, Yasuhiro K. Corrosion phenomenon and its analysis of 6063 aluminum alloy in ethyl alcohol. Materials Transactions. 2009;50(6):1433–1439.

List of Symbols, Abbreviations, and Acronyms

3D	three-dimensional
AE-pSi	anodically etched pSi
Al	aluminum
$AlBr_3$	aluminum bromide
Ar	argon
atm	atmosphere
ATR	attenuated total reflection
Br	bromine
Cl	chlorine
Cr	chromium
FTIR	Fourier-Transform infrared spectroscopy
H	hydrogen
HF	hydrofluoric acid
MCT	mercury–cadmium–telluride
Mg_2Si	magnesium silicide
Na	sodium
NaCl	sodium chloride
$NaClO_4$	sodium perchlorate
Ni	nickel
NiCr	nichrome
O	oxygen
pSi	porous silicon
SEM	scanning electron microscopy
XRD	X-ray diffraction

1 (PDF)	DEFENSE TECHNICAL INFORMATION CTR DTIC OCA
1 (PDF)	DEVCOM ARL FCDD RLD DCI TECH LIB
3 (PDF)	DEVCOM ARL FCDD RLD D P GUERIERI FCDD RLS EM N BANEK W CHURAMAN
2 (PDF)	GEORGE WASHINGTON UNIVERSITY D ABELE M WAGNER
1 (PDF)	FIBERTEK K PRICE